Dear reviewers, dear editor,

please find the marked-up manuscript in the following pages. Major changes as proposed by reviewer 1: The static GRACE gravity field solution is replaced by the monthly GRACE RL06 JPL solution. The abstract, introduction and conclusions section is changed to specify the results.

Minor changes:
- Fig. 7: now shows the ROTI weights.
- Fig. 8: gravity fields are evaluated up to degree 70. Now indicated in the caption
- Most of the figures are replaced by updated versions with better font size and correct labels.

Two short sections describing the orbit processing and the gravity field computation have also been included.

Best regards,
Lucas Schreiter

Mitigation of ionospheric signatures in Swarm GPS gravity field estimation using weighting strategies

Lucas Schreiter[1], Daniel Arnold[1], Veerle Sterken[1], and Adrian Jäggi[1]

[1]Astronomical Institute, University of Bern, Sidlerstrasse 5, 3001 Bern, Switzerland

Correspondence: Lucas Schreiter (lucas.schreiter@aiub.unibe.ch)

Abstract. Even though ESA's three-satellite low earth orbit (LEO) mission Swarm is primarily a magnetic field mission, it ~~became more and more important as~~ can also serve as a gravity field mission. Located in a ~~low earth orbit with altitudes of 460km~~ LEOs with initial altitudes of 480 km for Swarm A and Swarm C and ~~530km~~ 530 km for Swarm B ~~, after the commissioning phase,~~ and equipped with geodetic-type dual frequency ~~GPS~~ Global Positioning System (GPS) receivers, it is suitable for gravity field computation. Of course, the Swarm GPS-only gravity fields ~~are not as good as~~ cannot compete with the gravity fields derived from the ~~ultra precise GRACE~~ ultra-precise GRACE (Gravity Recovery And Climate Experiment) K-Band measurements~~, but due to~~. But for various reasons like the end of the GRACE mission in October 2017, data gaps in the previous months due to battery ageing, and the gap between GRACE and the recently launched GRACE Follow-On mission, Swarm gravity fields became important to maintain a continuous time series and to bridge the gap ~~. By validating the Swarm gravity fields~~ between the two dedicated gravity missions. By comparing the gravity fields derived from Swarm kinematic positions to the GRACE gravity fields, systematic errors have been observed in the Swarm results, especially around the geomagnetic equator. These errors are already visible in the kinematic ~~positioning~~ positions as spikes up to a few centimeters from where they propagate into the gravity field solutions.

We investigate these systematic errors by analyzing the geometry-free linear combination of the GPS carrier phase observations and its time derivatives using a combination of a Gaussian filter and a Savitzky-Golay filter and the Rate of TEC Index (ROTI). Based on this, we present different weighting schemes and investigate their impact on the gravity field solutions in order to assess the success of different mitigation strategies. We will show, that a combination of a derivative based weighting approach with a ROTI based weighting approach is capable of reducing the geoid RMS from 21.6 mm to 12.0 mm for a heavily affected month and that almost 10 % more kinematic positions can be preserved compared to a derivative based screening.

1 Introduction

Even though Swarm was designed as a magnetic field mission, Swarm ~~became~~ has become important as a gravity mission to bridge the gap between ~~Grace and Grace Follow On (Lück et al., 2018). The GRACE K-Band gravity fields were ultra~~

~~precise~~GRACE and GRACE Follow-On (Lück et al., 2018). Thanks to the ultra-precise inter-satellite K-band measurements and high-quality accelerometer data, GRACE-derived gravity field models are of superior quality, but due to battery aging starting in 2011, they started having gaps and ~~finally~~ eventually no more GRACE gravity fields were available since June 2017. The GRACE mission ended in October 2017 ~~. GRACE Follow-On~~ (JPL/NASA, 2017). GRACE Follow-On was launched on May 22, 2018~~, resulting~~ . Due to a failiure in the microwave instrument a switchover to the backup system had to be performed the science phase is expected to start in January 2019 (JPL/NASA, 2018). This results in a gap of ~~more than half a year~~1.5 years.

Recent comparisons of GRACE (~~K-Band~~K-band) gravity fields to Swarm (GPS-only) gravity fields showed two pronounced band shaped artifacts of about ~~$4cm$~~ 4 cm in geoid height along the geomagnetic equator ~~,~~ when adopting a ~~gauss filter of $500km$~~ Gaussian filter of 400 km (Jäggi et al., 2016). A similar behavior of LEO based GPS-only gravity fields was observed earlier in the computation of GOCE (Gravity Field And Steady-State Ocean Circulation Explorer) GPS-only gravity fields (Jäggi et al., 2015). In the GOCE case only the ascending arcs (~~$\sim 18h$~~ ~ 18 h magnetic local time (MLT)) showed this behavior due to the dusk-dawn orbit configuration of the GOCE satellite (Bock et al., 2014). This special ~~MLT~~ MLT is well-known for a very pronounced equatorial ionization anomaly, equatorial spread F, as well as equatorial plasma bubbles (Whalen (2000), Stolle et al. (2006)). In this region high gradients exist in the plasma density, which in turn may affect the tracking.

Usually for the GPS-based kinematic positioning the ionosphere-free linear combination

$$L_{IF} = \frac{1}{f_1^2 - f_2^2} \cdot (f_1^2 L_1 - f_2^2 L_2) \qquad (1)$$

is used, where ~~f_1 and f_2~~ $f_1 = 1575.42$ MHz and $f_2 = 1227.60$ MHz are the carrier frequencies and L_1 and L_2 are the two GPS carrier phase observables. By ~~this first order terms~~ forming this difference the first order term of the ionospheric phase advance cancels out. The remaining parts tend to be very small and were found to be negligible for the presented investigation (Jäggi et al., 2015).

The differences between the Swarm and GRACE gravity fields significantly improved with the ~~tacking~~ tracking loop updates of the GPS receivers performed by ESA ~~(Dahle et al., 2017)~~(Dahle et al. (2017), van den IJssel et al. (2016)), which is an indicator, that the high ionospheric activity affects the receiver tracking and in turn contaminates the ionosphere-free linear combination.

In contrast to the sun-synchronous GOCE orbit, where only ascending arcs (close to 18 h MLT) were affected due to the dusk-dawn orbit geometry (Jäggi et al., 2011a), the Swarm orbit is evolving in ~~MLT, and a separation in ascending and descending arcs would therefore not fix the local time~~MLT, so the dependency of the artifacts on local time can be examined. ~~Therefore we prefer to~~ We use ionospheric information ~~,~~ directly derived from the GPS measurements. Such an approach was already successfully ~~used~~ applied by Jäggi et al. (2016) using epoch differences (a numerical approximation to compute the first time derivative) of the geometry-free linear combination

$$L_{GF} = L_1 - L_2. \qquad (2)$$

In case the absolute value of the derivative exceeded ~~$0.02m/s$~~ 0.02 ms^{-1}, the GPS observations were rejected. Even though it successfully removed most of the signatures, the orbit was ~~weakned~~ weakened due to the increased number of ambiguity parameters caused by gaps around the geomagnetic equator, as we will show later. In this article, we present a refined approach by using weighting strategies and assess if higher order time derivatives ~~may be an even~~ of L_{GF} may even represent a more adequate criterium to identify the problematic GPS data.

2 ~~Systematic errors in kinematic positioning~~Impact of the ionosphere on GPS tracking performance

2.1 Swarm precise orbit determination

The Precise Orbit Determination (POD) was performed using the Development Version 5.3 of the Bernese GNSS Software. We are following the procedure published in (Jäggi et al., 2016). As external products, the final GPS orbits and the high-rate 5-s GPS satellite clock corrections are used, which are provided by the Center Of Orbit Determination Europe (CODE). The Swarm Level-1b Receiver Independent Exchange Format (RINEX) 3 data (Gurtner and Estey, 2007) and Level-1b attitude data derived from the star tracker cameras are used. A final reduced dynamic orbit with 6 min. piecewise constant accelerations and a kinematic orbit are computed from undifferenced GPS carrier phase observations. Code observations are only used for the initial clock synchronization. For the reduced dynamic orbit the gravity field model EGM2008, together with the ocean tide model FES2004 are used. No non-gravitational forces were modeled. Both orbit types are computed for 24 h orbital arcs. Kinematic positions are essential for the gravity field determination as they contain no a priori information about the LEO's dynamics. Phase Center Variation (PCV) maps were generated in-flight using a residual approach. Ionosphere-free phase residuals larger than 4 cm compared to a screening orbit with 15 min. piecewise constant accelerations are removed in the preprocessing. Usually for reduced dynamic and kinematic orbit determination the phase observations have the same weight $p = \frac{\sigma_0^2}{\sigma^2}$ where σ_0 is the a priori sigma for L1 phase observations of 1 mm and σ usually also equals 1 mm. For weighting, we will assign a specific σ to each observation. The ionosphere-free phase residuals, as shown in Fig. 2 and 7, were computed by using the screening orbit without rejecting large phase residuals. The same residuals were used to select the thresholds for weighting.

2.2 Systematic errors in kinematic positioning

It was shown in earlier studies (~~(Jäggi et al., 2016), (Dahle et al., 2017)~~Jäggi et al. (2016), Dahle et al. (2017)) that the artifacts in the gravity field solutions are caused by the ionosphere. For that reason we link ~~excursions in the kinematic positions~~ fast changing differences between kinematic positions and a reduced dynamic orbit to the ambient plasma density. Swarm is ~~eqipped with a~~ equipped with Langmuir probes to directly measure in-situ plasma density. Figure 1 shows a comparison between the ~~the~~ measured plasma density and differences of kinematic positions to a reduced dynamic orbit, which is offering more dynamical stiffness and thus less susceptible to ionospheric disturbances. Especially around the sharp peak in plasma density, jumps of up to ~~four~~ a few centimeters are observed in the orbit differences. If one compares this to the ionosphere-free GPS phase residuals at the respective epochs, see ~~figure~~ Fig. 2 (top), ~~their~~ the epoch wise variance over all GPS-satellites is

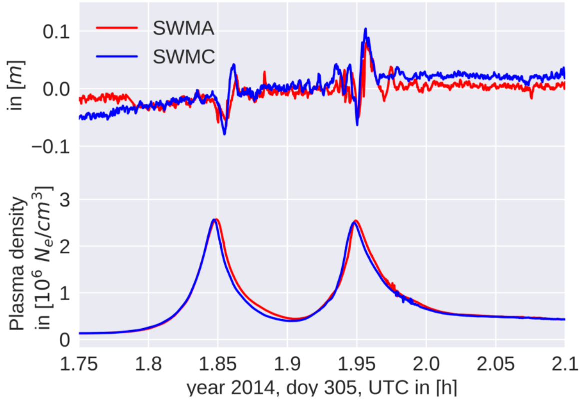

Figure 1. Orbit differences in the radial component between kinematic positions (KN) and a ~~reduced-dynamic~~ reduced dynamic (RD) orbit fit (top) and plasma density during an equatorial pass.

getting larger~~(widening), indicating a~~ , indicating an inconsistency in the phase observables. ~~The receiver clock is estimated such that the epoch wise mean of the phase residuals gets minimized. For that reason the ionosphere-free phase residuals are not independent for different GPS satellites.~~ The ~~widening~~ degradation occurs at the same epochs, where the measured plasma density has its peaks (see ~~figure~~ Fig. 1 and 2 top curves). Because the GPS-receiver is moving with a large velocity (about ~~7.7km/s~~7.7 km s^{-1}), large gradients in the plasma density are clearly reflected in the geometry-free linear combination. Due to the different line-of-sights to the tracked GPS-satellites, this geometry-free linear combination has a large spatial variability. In the following, we establish criteria for the occurence of the ~~widening~~ degradation in the ionosphere-free phase residuals. We use ~~its numerical derivatives~~ numerical derivatives of the geometry-free linear combination, because the ~~widening~~ degradation seems to be associated with rapid changes in plasma density and thus in the geometry-free linear combination. The geometry-free linear combination can be computed directly from the GPS RINEX file. No additional information, e.g., an a priory orbit based on an underlying gravity field, is needed. ~~The ionosphere-free phase residuals, as shown in figures 2 and 7, were computed by using a reduced dynamic orbit with 15 min piecewise constant accelerations. The same residuals were used to define the thresholds used in the following. For the orbit computations the Bernese GNSS software package V5.3 was used (Dach et al., 2015). In all cases a standard GPS phase screening was performed, rejecting large ionosphere-free phase residuals ($> 4cm$). This is consistent with the standard orbit processing at the Astronomical Institute of the University of Bern (AIUB).~~

2.3 ~~Kinematic covariances~~Radial variances

The ~~the covariance information~~ covariance information of the kinematic point positioning may be used as an indicator for the quality of kinematic positions. Based on this, the kinematic positions may be weighted in the subsequent for gravity field ~~processing~~determination. As shown by Jäggi et al. (2011b), however, this basically represents the geometry of the observation ~~.~~ ~~If affected epochs~~ scenario. If kinematic positions have a high covariance ~~they do not propagate into~~ their impact on the gravity

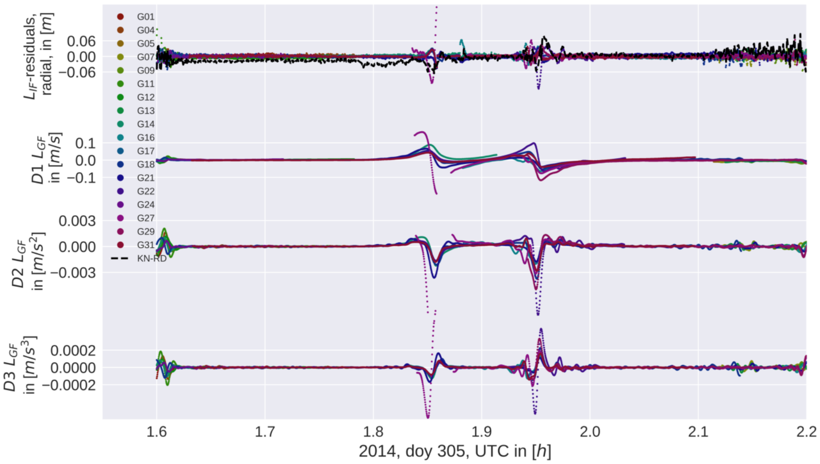

Figure 2. Phase residuals in ~~kinematic~~ reduced dynamic positioning (top) and time derivatives of the geometry-free linear combination during one equatorial pass.

field solutions is small, because they get properly weighted according to the covariance information. Because we saw in Sect. 2.2, that the spikes are associated with a spreading of the ~~Phase~~ phase residuals, we compare the kinematic covariance with the ~~epoch wise~~ epoch-wise standard deviation of the phase residuals ~~, see figure~~ over all satellites, see Fig. 3. We use magnetic latitude and magnetic local time because the ~~phenomena~~ phenomenon is most prominently visible around the magnetic equator in the evening hours. For the kinematic radial variances we used the formal error propagation in radial direction,

$$\sigma_r{}^2 = (1/r^2)\cdot(x^2\cdot k_{xx} + y^2\cdot k_{yy} + z^2\cdot k_{zz} + 2\cdot x\cdot y\cdot k_{xy} + 2\cdot x\cdot z\cdot k_{xz} + 2\cdot y\cdot z\cdot k_{yz}),$$

where x, y and z are the coordinates in an earth fixed system and k_{xy} denotes the covariance between x, y and ~~r is the radius~~$r = \sqrt{x^2+y^2+z^2}$ is the geocentric distance. We use this to represent the quality of the 3D-positions in radial direction, whereas we used the standard deviation of the phase residuals over all satellites at a certain epoch. These values were binned, the mean of each box was computed, and for the purpose of visibility the logarithm was used for the kinematic variances. ~~Both pictures~~ The two figures look very different, especially around the polar regions, where large phase residuals are more frequently observed. A different behavior can also be seen around the geomagnetic equator. In this region the high standard deviation in phase residuals is also affecting earlier local times, and in slightly different latitudes, than the high variances in kinematic positioning. For both plots the same months (analyzed test period: 2015: Jan., Mar.; 2016: Feb., Mar., Jun., Jul., Aug.) were used and only kinematic positions with a minimum redundancy of 5 GPS-satellites were used. No additional weighting or screening was performed.

As shown by Xiong et al. (2016), the loss of locks of the Swarm GPS receivers are highly correlated to bubble events. Whereas loss of lock corresponds to the worst case scenario, we saw in ~~figure~~ Fig. 3, that the kinematic radial variances also

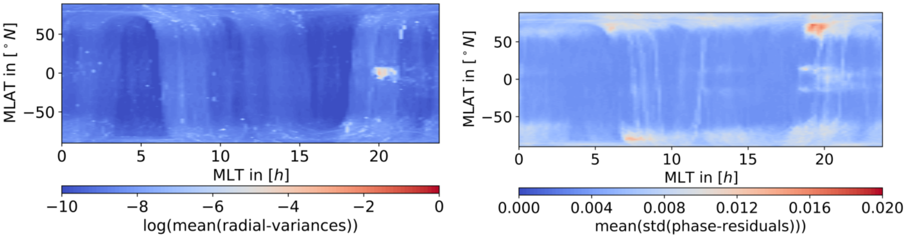

Figure 3. ~~Kinematic~~ Radial variances (left) and spreading of phase residuals (right) binned in magnetic coordinates for the analyzed test period.

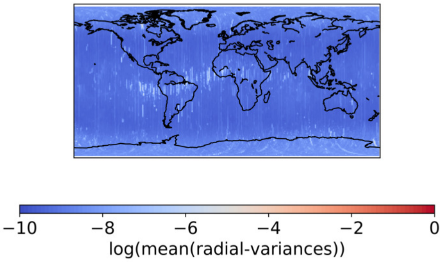

Figure 4. ~~Kinematic covariances~~ Radial variances binned for a longer timespan in geographic coordinates, Nov. 2013 - Dec. 2017

generally increase in the potential bubble regions, i.e. after sunset ($18-22$ MLT) and near the geomagnetic equator. In this study we extend the investigations by checking the ~~covariances~~ radial variances of the unweighted and un-screened kinematic positions for Swarm for a long time span. As shown in the previous section, the phase residuals increase around the peaks in plasma density, indicating a potential degradation of the phase observables or a weaker geometry due to screened GPS-observations or possible loss of locks.

In ~~figure~~ Fig. 4 we binned the ~~covariances in $1°lon \times 1°lat$~~ radial variances in 1° lon ×1° lat and formed the average using unweighted kinematic positions ~~form~~ from $11/2013-12/2017$ and all three Swarm ~~Satellites~~satellites. Only positions with ~~enough~~ sufficient redundancy were used. Figure 4 shows that the geomagnetic equator is clearly visible showing the largest ~~covariances~~radial variances. If one reproduces this plot in ~~MLT and $Mlat$, compare figure~~ MLT and Mlat, compare Fig. 3 (left), a very pronounced peak around ~~$18-22hMLT$~~ $18-22$ h MLT gets visible around ~~$0Mlat$~~0° Mlat. It should be noted, that the time span used for ~~figure 3 is~~ Fig. 3 is given by the analyzed test period and by this it is shorter than in ~~figure~~ Fig. 4. Nevertheless, the observed patterns are almost identical to the results of Xiong et al. (2016), even if loss of locks or data gaps for all GPS-satellites are by construction not included in our figures. This again supports the statement, that the GPS data quality suffers significantly from high activity in the magnetic-equatorial ionosphere at evening hours and, of course, due to equatorial plasma bubbles (see ~~figure~~ Fig. 3 (left)).

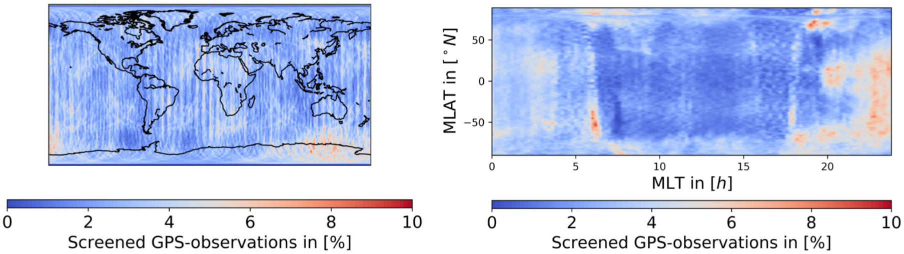

Figure 5. Average number of GPS-observations screened in the preprocessing for the analyzed test period. Left: geographic coordinates, right: magnetic coordinates

2.4 Screened observations in preprocessing

In the ~~standard~~ orbit processing some observations are rejected in the preprocessing, because they are considered as outliers, show large phase residuals, due to gaps, or small observation pieces. This screening is performed to avoid ~~the propagation of data problems~~ that data problems propagate into the orbit solution. Even though this screening process applies especially in the night time hours, it does not seem to detect the observations responsible for the spikes in the kinematic positioning. The mean number of observations screened in the preprocessing is shown in ~~figure~~ Fig. 5. As before only valid kinematic positions with enough redundancy were used and the mean difference between the number of observations in the RINEX file and the observations used for the final kinematic positioning is shown.

2.5 Computation of derivatives

Due to the noise of the geometry-free linear combination the computation of meaningful derivatives is not straightforward. In order to obtain reliable derivatives we use a combination of a Gaussian filter and a Savitzky-Golay filter. First, we smooth our data with the Gaussian filter, then we apply the Savitzky-Golay filter to obtain the next order derivative, we smooth again, etc.. This approach allows us to keep the ~~windowsize~~ window size and the degree for the Savitzky-Golay filter low and by this ~~attenuate~~ reduce the sensitivity to noise in the higher order derivatives. Before applying the filters, we use a jump and outlier detection with a threshold of ~~$0.5m/s$~~ $0.5\ \mathrm{m\,s^{-1}}$, applied on epoch differences of the geometry-free linear combination. If larger jumps occur, the arcs were split to avoid any contamination of the derivatives. This action was also performed ~~if there were~~ in case of gaps of one or more epochs in the ~~$1Hz$~~ $1\ \mathrm{Hz}$ RINEX data. For the Gaussian filter we select a bandwidth of ~~$10s$~~ $10\ \mathrm{s}$, a symmetrical window with a total width of ~~$10.1s$ and min. number points~~ $10.1\ \mathrm{s}$ and minimum number of 10 points. For the Savitzky-Golay filter we choose a polynomial of degree 1, a symmetrical window with a total size of ~~$12.5s$ and a min. number of points of~~ $12.5\ \mathrm{s}$ and a minimum number of 7 points. The parameters were determined empirically using an artificial signal (~~figure~~ Fig. 6) and original Swarm RINEX data. Especially in case of the Gaussian Filter it is important to choose the parameters such that the window is almost ~~full~~ fully populated (with the mentioned setting: max. one epoch missing) and symmetrically occupied, otherwise we may bias the smoothed points to the mean of the previous ones, and ~~pushing~~ forcing the derivatives to zero. If it was not possible to compute the derivative due to ~~gaps or~~ jumps, gaps or not enough data, the corresponding epochs were marked to ~~handle them separately at a later~~ set weights manually in a latter stage. In our ~~case~~ processing we will downweight these epochs.

In ~~Figure~~ Fig. 2 we show a short time series of phase residuals and the corresponding derivatives during one equatorial pass. It may be seen that the second and third time derivative are more focused to the epochs where the spikes ~~occure~~ occur than the first time derivative. The higher derivatives show comparatively larger amplitudes at the boundaries, which correspond to the polar regions, indicating, that the quality of the derivatives might suffer from observation noise.

To check the consistency of the adopted differentiating schemes and to validate them, we simulated a signal including random jumps, observation gaps and random noise. The ~~Signal~~ signal was simulated by $f(t) = \sin((100t)^2)$ where t is measured in days. A Gaussian noise with a standard deviation of ~~$5cm$~~ 5 cm was selected. The number of jumps and the number of gaps was set to 40 and the locations were determined randomly. The jump sizes are given by a Gaussian random variable with a standard deviation of ~~$5m$~~ 5 m and the length of gaps in seconds is determined by a Poisson random variable with $\lambda = 100$. The ~~Signal~~ signal was chosen to ~~have different frequencies with~~ be represented by a sinusoidal signal with frequencies changing as a function of time, allowing to evaluate the performance of the differentiating scheme with frequency. In ~~Figure~~ Fig. 6 we compare the following two cases. We compute the derivatives in the first case with an almost non smoothed differentiating scheme using no Gaussian filter and only three points for the ~~Salvitzky-Golay~~ Savitzky-Golay filter, and with the parameters mentioned above. If the smoothing is too weak, as one can see in the three-point case, the derivatives are very noisy. With the stronger smoothing one gets a dampening of the higher frequencies (approximately 10%,15% and 25% for the first,second and third derivative at ~~$0.015Hz$~~0.015 Hz), but in total the derivatives obtained ~~represents~~ represent the true derivative, as may be seen in ~~figure~~ Fig. 6. The gaps in the derivatives are given by artificial gaps in the data, but were further enlarged due to the min. number of points restriction.

3 Weighting of Observations

3.1 AIUB standard screening

As a reference the AIUB standard screening is used, as published in (Jäggi et al., 2016)~~is used~~. It successfully removed the ~~signatures~~artifacts, although the orbit quality was weakened and the number of ambiguities increased. Because it is a derivative based approach it can be used as a direct reference to our weighting solutions. In the AIUB standard screening the first time derivative of the geometry-free linear combination is computed without any smoothing using the ~~half difference~~ half-difference of the previous and the next epoch, which is ~~equivalentot~~ equivalent to the three point differentiating scheme shown in ~~section 2.4~~Sect. 2.5. Comparing this method to our differentiating scheme, compare ~~figure 6, the~~ Fig. 6, differences are visible, but both derivatives show similar amplitude and shape. If the absolute value of the first time derivative exceeded ~~$2cm/s$~~2 cm s^{-1}, the observation was removed from the RINEX observations file. This introduces data gaps which are mostly responsible for the increased number of ambiguity parameters due to a very conservative setting up of new ambiguity parameters if data gaps

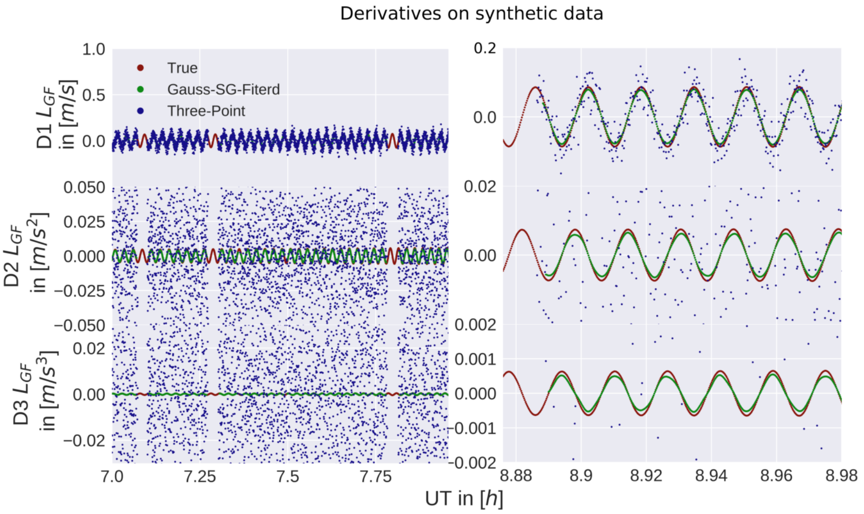

Figure 6. Tests on synthetic data. Red points ~~indicates~~ show the true analytic noise-free derivative, green the computed derivatives from noisy data using the filter settings from ~~section 2.4~~ Sect. 2.5 and blue points the three point derivative scheme. The noise in the second and third plot visible in the blue points exceeds the limit of the axis. The right side shows a zoom to compare the true derivative with the Gauss-SG filtered derivative.

are longer then 61 ~~sec.~~seconds. In cases, where too many observations had to be removed, the kinematic positions could not be computed anymore.

3.2 Derivative based weighting

In the derivative based weighting schemes, we tested the first, second and third time derivative. As mentioned in ~~section 2.4~~ Sect. 2.5, we use a combination of a ~~Gaussian- and a Savitzky-Golay-filter~~Gaussian and a Savitzky-Golay filter. This additional effort is necessary due to noise of L_{GF}. As shown in ~~section 2.4~~ Sect. 2.5 already for the second time derivative using a classical three-point differentiation scheme, one would basically only see noise.

After ~~computing the numerical~~ numerically computing the time derivatives, we apply empirical thresholds. These thresholds were set by checking the amplitude of the derivatives, evaluating the performance on the gravity field level, and the threshold used by (Jäggi et al., 2016). The thresholds were set to ~~$2\mathrm{cms}^{-1}$ for $\frac{dL_{GF}}{dt}$, $0.025\mathrm{cm\,s}^{-2}$ for $\frac{d^2L_{GF}}{dt^2}$ and $0.00075\mathrm{cm\,s}^{-3}$ for $\frac{d^3L_{GF}}{dt^3}$~~ $2\ \mathrm{cm\,s}^{-1}$ for $|\frac{dL_{GF}}{dt}|$, $0.025\ \mathrm{cm\,s}^{-2}$ for $|\frac{d^2L_{GF}}{dt^2}|$ and $0.00075\ \mathrm{cm\,s}^{-3}$ for $|\frac{d^3L_{GF}}{dt^3}|$.

If the time derivative at a certain epoch exceeds the threshold, an observation specific ~~σ of 21 (standard $\sigma + 20$~~σ^2 of $21\ \mathrm{mm}^2$ (standard $\sigma^2 + 20\ \mathrm{mm}^2$) is given to the observation instead of a standard unweighted ~~σ of 1~~σ^2 of $1\ \mathrm{mm}^2$. This kind of extreme down-weighting is used to have a similar impact on the orbit as the standard screening, but because the observations stay in the RINEX observation file and also in the resulting normal equation system, no gaps are introduced and no additional ambiguities that ~~are weakening~~ would degrade the orbit. In case an observation epoch was too close to a gap or a jump and no derivative could be computed, the data point was ~~down weighted in addition~~downweighted in addition, assuming that the observation might be affected. The third time derivative suffers most from enlarged gaps due to non-computable derivatives~~and~~. The gravity field recoveries based on correspondingly generated kinematic orbits turned out to be of inferior quality. For that reason, we focus on the first and second time derivative in the following sections.

For the first time derivative we set the ~~thresold~~ threshold to obtain similar results as with the AIUB standard screening to have a zero-test and to gain additional insight in the difference between screening and weighting. This ~~as intended to perform as kind of zero-test and also giving hint to~~ is intended to directly assess the differences between screening and weighting.

3.3 ROTI based weighting

The ROTI (Rate Of ~~TEC~~ Total Electron Content (TEC) Index) based weighting was used by Zehentner and Mayer-Gürr (2015) for the GOCE orbit processing, where similar issues have been observed by Jäggi et al. (2015). ROTI is defined as

$$ROTI = \sqrt{\frac{\langle \Delta TEC^2 \rangle - \langle \Delta TEC \rangle^2}{\Delta t^2}} \tag{3}$$

and is applied ~~in~~ as a sliding window ~~manner~~ (Pi et al., 1997). The window size is set symmetrically with a width of ~~$31s$~~31 s. The differences to determine the ΔTEC were computed using the previous and the current epoch:

$$\Delta TEC(t_i) = TEC(t_i) - TEC(t_{i-1}) \tag{4}$$

In analogy to Sect. ~~3.2 the~~ 3.2 points were downweighted with a sigma ~~of 21~~ square of 21 mm^2 if the number of data points was below a threshold of 10. For the ROTI approach, we tested two different scaling functions. First, we used the scaling function applied by Zehentner and Mayer-Gürr (2015) for GOCE, which reads ~~as $\sigma = max(1, 20 \cdot ROTI)$~~$\sigma^2 = max(1, 20 \cdot ROTI)\ \mathrm{mm}^2$. This approach, however, turned out not to have an impact on the Swarm ~~Data~~data. For our tests, we therefore modified the weighting according to

$$\sigma^{AIUB\,2}_{\underline{ROTI}\,\underline{AIUB-ROTI}} = max(1, 60 \cdot ROTI)\ \mathrm{mm}^2. \tag{5}$$

~~or alternatively as proposed for Swarm, private communication~~Alternatively, N. Zehentner, 2017 (private communication) proposed for Swarm the following scaling function:

$$\sigma^{GRAZ\,2}_{\underline{ROTI}\,\underline{GRAZ-ROTI}} = exp(20 \cdot ROTI)\ \mathrm{mm}^2. \tag{6}$$

In case the ~~ROT-Index~~ ROTI is small, both approaches should return a ~~σ close to 1~~σ^2 close to 1 mm^2. In case of high fluctuations, where ROTI gets large, the second weights are much larger. The first set of weights will be referred ~~as ROTI 1~~to as AIUB-ROTI, the latter as ~~ROTI 2.~~ Graz-ROTI. As one can see in ~~figure~~ Fig. 7 the ROTI weights are particularly pronounced in regions where ~~die~~ the ionosphere-free phase residuals are large. ROTI turned out to be most effective in the polar regions due to the presence of plasma density fluctuations.

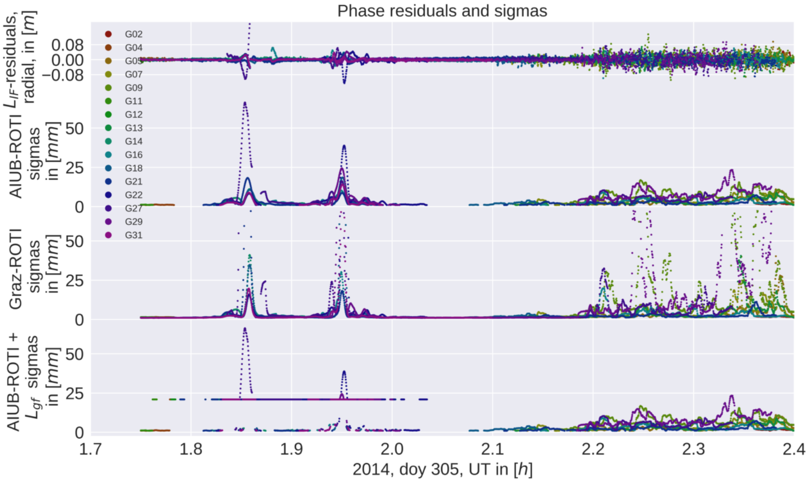

Figure 7. From top to bottom: Ionosphere-free phase residuals~~(top)~~, AIUB-ROTI ~~sigmas (middle)~~ sigma squares, Graz-ROTI sigma squares and AIUB-ROTI combined with the second derivative~~(bottom)~~. Around 1.9 UT there is an equatorial pass and around 2.3 UT a polar pass. The ROTI ~~sigmas~~ sigma squares are ~~very present~~ larger at the polar region, the second derivative with a fixed sigma square (bottom) is ~~more restrictive at~~ only used near equatorial regions. Only sigma squares unequal 1 mm^2 were plotted.

3.4 ~~Localizing the weights~~Geographical restriction of downweighting

We are aiming to reduce the impact of the artifacts induced by the equatorial ionosphere on the gravity ~~fields~~ field models and consequently improve ~~the qualityof the obtained gravity fields~~their quality. Some of our derivative-based approaches led to a degradation of the gravity fields in the polar regions as it will be shown in ~~section 4.1~~Sect. 4.2. To avoid this degradation we are limiting our ~~derivative based~~ derivative-based weighting to equatorial regions with a latitude between ~~$-50° N$ and $50° N$~~ $-50°$ N and $50°$ N. Due to the shape of the geomagnetic equator (which is located between roughly ~~±13°~~±13° lattitude) and the ~~of the~~ equatorial ionization anomaly, which is located between ~~$-20 Mlat$ and $20 Mlat$~~ -20 Mlat and 20 Mlat (Whalen, 2000), this covers all the equatorial ionosphere. For the ROTI approaches no such limitation was performed due to the positive effect in the polar regions. The localized weighting will be referred to as equatorial (eq.).

3.5 Combination of Methods

~~Because the ROTI weighting is powerful at~~ In the polar regions ~~and the derivative based weighting in~~ the ~~equatorial regions, we~~ ROTI approach performs better, compare Fig. 8. The derivative based approaches are more powerful in removing the equatorial artifact. Conclusively it is natural to combine both methods. Because the scaling function in case of the ~~AIUB-scaled ROTI 1~~ AIUB-ROTI provides less extreme weights, we decided to combine this one ~~to~~ with the second derivative. This is achieved by taking the maximum of the ~~ROTI-sigma~~ AIUB-ROTI sigma square and the second derivative based sigma square in the equatorial regions, compare ~~figure~~ Fig. 7.

4 Evaluation

4.1 Gravity field determination from kinematic positions

The celestial mechanics approach is used for gravity field determination as described in Jäggi et al. (2016) Jäggi et al. (2011a) and Beutler et al. (2010). In this procedure first 24 h arc a priori orbits are generated using the kinematic positions as pseudo-observations which are weighted epoch-wise using their formal covariance information. For the a priori orbits the gravity field model EGM2008 and the ocean tide model FES2004 is applied. Empirical accelerations are used to compensate the non-gravitational forces. Swarm accelerometer data were not taken into account for the gravity field determination. The orbits are then expressed as truncated Taylor series including the empirical accelerations and the spherical harmonic coefficients of the gravity field. Daily normal equations (NEQ) are then set up, the empirical accelerations are pre-eliminated, and the daily NEQs are stacked in order to obtain monthly NEQ which eventually is inverted. By solving the NEQ corrections of the spherical harmonics coefficients with respect to the a priori gravity field are obtained. No regularization is applied in this article.

4.2 Swarm gravity field recovery

In order to validate our gravity field ~~reovery~~ recovery results, we use the ~~static AIUB-GRACE03S~~ monthly JPL-GRACE-RL06 gravity field model as a reference field. Due to the ultra-precise ~~K-Band~~ K-band inter-satellite measurements the GRACE gravity fields are of very high quality and essentially free from systematic ionospheric errors. ~~In figure~~ GRACE GPS only gravity fields are also free from systematic ionospheric errors, but in many observations are missing around the geomagnetic equation in the GRACE RINEX files (Jäggi et al. (2016), Fig. 12).In Fig. 8 (top left) we computed the geoid height differences between the ~~AIUB-GRACE03S~~ JPL-GRACE-RL06 gravity field and a monthly Swarm GPS only gravity ~~fields using the un-screened and~~ field using the unweighted orbits. The ~~specific month, march~~ differences were computed by taking the gravity fields up to degree and order 70 into account. The displayed month, March 2015, is heavily affected by the artefacts. The stripes around the geomagnetic equator are clearly visible with an amplitude of ~~around 4*cm*~~ approximately 4 cm in geoid height when adopting a Gaussian filter radius of ~~500*km*~~400 km. In case of the gravity fields obtained using the AIUB standard screening (top, right), these two bands have virtually disappeared.

As a first step we compare the AIUB standard screening with the weighting based on the first derivative. This zero test shows a similar performance as the standard AIUB screening, but especially in ~~the pacific region~~ near Columbia and east of south america it seems to add some additional artifacts. Figure 13 explains the different behavior, if we compare ~~to~~ the number and location of the positions that were actually used for the gravity field recovery. The standard screening removes almost all positions in that specific area, in contrast to the weighting, were the positions are preserved, but minor artifacts appear instead. ~~In order to remove the two bands we see ,~~ We see that the second derivative has a similar performance ~~w.r.t.~~ when compared to the AIUB standard screening. In particular also the artifact in the pacific region vanished. In contrast to the standard screening, the noise seems slightly reduced, which may be seen in Fig. 8 and Table 1 and 2 when comparing the geographically weighted RMS of geoid height differences and the weighted standard deviation over the ocean. Using the second derivative with no geographical restrictions, we see some larger fluctuations around the polar regions. For this reason, we limit the second derivative based weighting to the equatorial regions.

~~In removing the two bands both~~ The ROTI approaches are not very successful ~~, but concerning~~ in removing the two band around the geomagnetic equator. In the polar regions, however, the ROTI based gravity fields show reduced noise~~. This impression~~, see Fig. 8. The noise reduction of the ROTI approaches may be seen when comparing the geoid RMS as well as the weighted standard deviation in Tables 1 and 2. This is supported by the ~~degree difference~~ difference degree amplitudes shown in ~~figure~~ Fig. 9. For degrees above ~~25 the degree differences~~ 25 the difference of both ROTI approaches are among the lowest. ~~A different picture results, howver, gets visible if one focuses on the degree differences between~~ This implies that small scale fluctuations are successfully reduced. A different result is obtained from degree 15 ~~and~~ to 25. In ~~these degrees~~ this spectral band the performance of the derivative based screening and weighting approaches clearly outperforms the ROTI solutions. ~~These degrees are the specific degrees, where the equatorial artifact is located in.~~

If one compares the AIUB screening to the second derivative, the AIUB screening shows a slightly better performance in the low degrees (< 10) but in most of the higher degrees the ~~latter one~~ new approach shows a similar or even better performance.

~~Because the second derivative proofed very successful in removing the artifact, and the ROTI approach is most effective in reducing the noise and improving the gravity field in polar regions, it makes sense to combine both. For this purpose~~ Eventually we tested a combination of ~~ROTI 1~~ AIUB-ROTI and the second derivative limited to the equator using the maximum sigma ~~ob~~ square of both approaches. The differences in the gravity field, see ~~figure~~ Fig. 8, still show some increased noise around the geomagnetic equator, but it is about the same level we had with the second derivative based weighting. Especially ~~above~~ in the region over Greenland the gravity field benefits from the ROTI weighting. Looking again ~~to~~ at the degree difference amplitudes, the light blue line is ~~above~~ among the lowest for almost all degrees. ~~In total a combination seems to be most efficient and result into the best gravity fields in this comparison.~~

4.3 Weighted observations

It is our ambition to remove the equatorial artifact by down-weighting as few ~~epochs~~ observations as possible. In the derivative based cases we specified a clearly defined threshold~~.~~, which allows to decide if an observation needs to be downweighted or not.

However, the ROTI approach affects almost all epochs, even if most of the weights are ~~small~~close to 1 mm^2. To evaluate how many epochs are heavily down-weighted we therefore set thresholds to the ROTI derived weights, to identify which observations are assigned strong weights. For representation purposes we chose two different thresholds for ROTI-based weights: ~~$\sigma > 2$ and $\sigma > 5$~~$\sigma^2 > 2$ and $\sigma^2 > 5$.

In ~~Figure~~ Fig. 10 the percentage of weighted ~~Observations~~ observations is illustrated in geomagnetic coordinates. Even though the first and second derivative show a similar performance, the weights based on the first derivative ~~seems~~ seem to act more

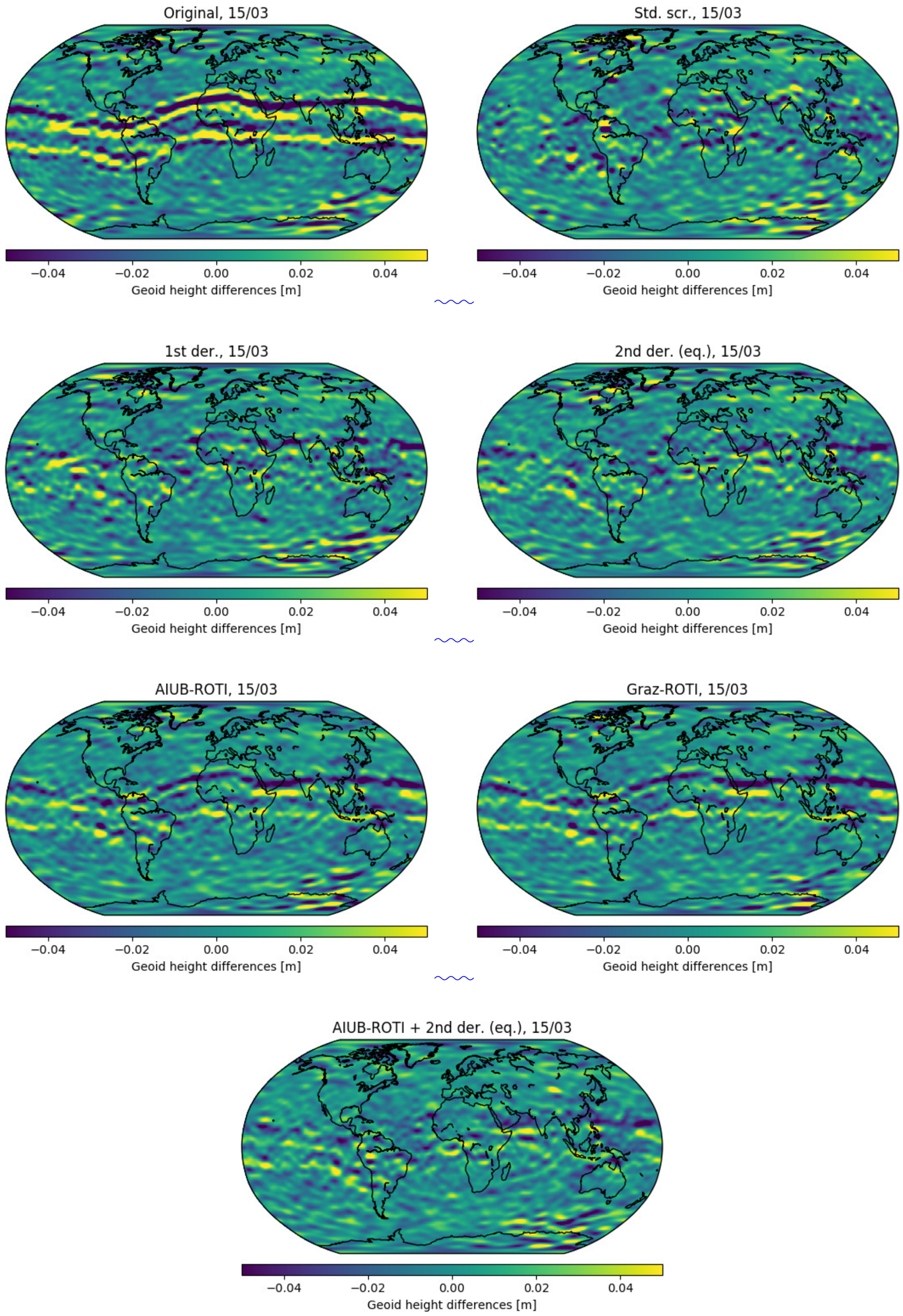

Original, 15/03

Std. scr., 15/03

1st der., 15/03

2nd der. (eq.), 15/03

AIUB-ROTI, 15/03

Graz-ROTI, 15/03

AIUB-ROTI + 2nd der. (eq.), 15/03

Figure 8. ~~Differences~~ Geoid height differences between monthly Swarm *A* gravity field to the ~~AIUB-GRACE03S~~ corresponding JPL-GRACE-RL06 solution for ~~march 2015~~March 2015. Gravity field differences were computed up to degree 70

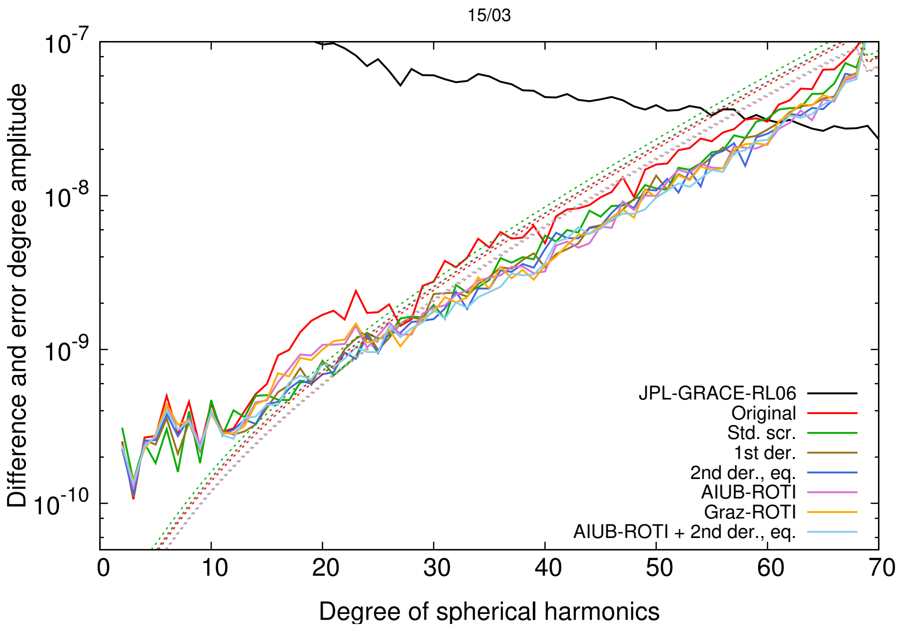

Figure 9. Difference (solid lines) and Error (dashed lines) degree Amplitude for monthly Swarm A gravity field w.r.t. AIUB-GRACE03S, ~~march 2015~~March 2015.

specifically on the outer boundary of the ~~Appleton anomaly~~ ionization crests than the weights determined by the second time derivative. Using the second derivative is therefore beneficial, if one assumes, that the spikes in the kinematic positions are aligned with the sharp peaks in plasma density and not on the flanks of the anomaly, which can be seen in ~~figure~~ Fig. 1. Evaluating the third time derivative one can see, that a too ~~high number of Observations gets weighted. Almost any~~ large number of observations gets down-weighted. Almost every observation around the pole is ~~touched~~affected, if no limitation to the equatorial region is applied.

The ROTI weighting approach is, however, much more sensitive to fluctuations in the geometry-free linear combination as they occur on the poles or due to equatorial plasma bubbles, but it is not as successful in removing the equatorial artifact. If one compares the ratio of weighted observations in ~~figure 10 for AIUB-ROTI>2 (middle left) and AIUB-ROTI>5~~ Fig. 10 for $\sigma^2_{AIUB-ROTI} > 2$ (middle right) and $\sigma^2_{AIUB-ROTI} > 5$ (bottom), the amount of weighted observations in the polar regions decreases significantly ~~with the increased threshold~~ when the threshold is increased. This implies that ~~to most of the observations not very large weights are assigned~~for most observations only small sigma squares are applied. This explains why the dynamic ROTI weighting shows such a good performance around the poles. It is able to identify noisy observations and therefore reduce high frequency noise in the gravity field solutions. The ROTI information is therefore to be used as a potential descriptor of the stochastic model of the GPS observations used for the positioning. Unfortunately the systematically biased positions in the equatorial regions can not ~~reliable~~ reliably be identified by a high ROTI value. This may be seen in ~~figure~~ Fig. 10 when comparing the plots in the top row to the plot at the bottom.

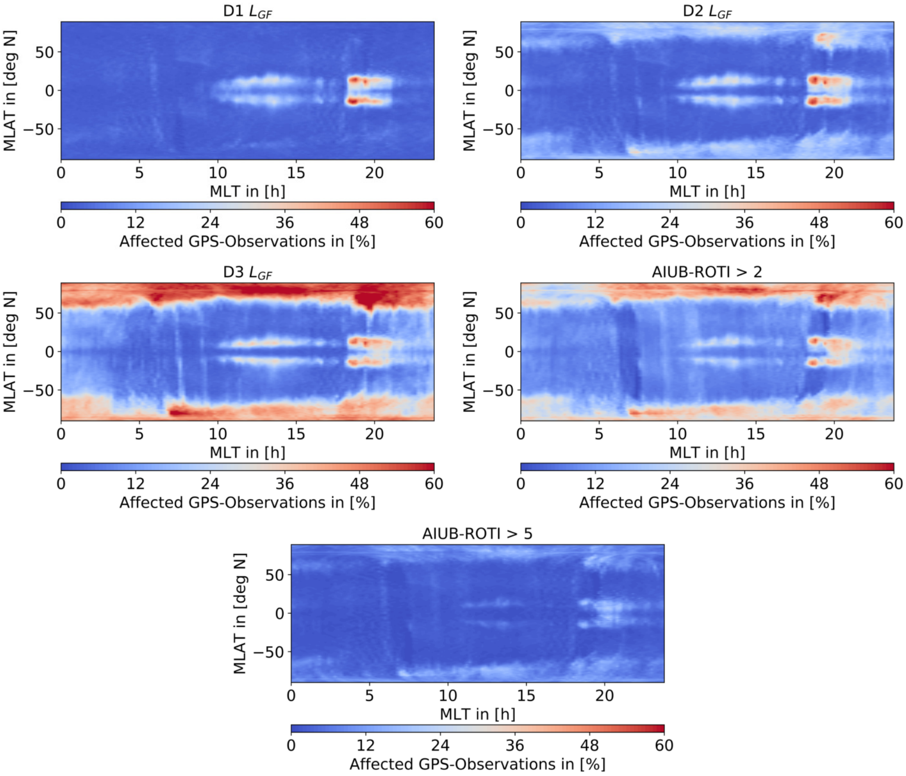

Figure 10. ~~Ratio~~ Ammount of weighted raw GPS measurements for the analyzed test period binned to the coresponding LEO position. Top: ~~D1-Cutoff~~D1-L_{GF}(left), ~~D2-Cutoff~~ D2-L_{GF}(right), middle: ~~D3-Cutoff~~ D3-L_{GF} (left), ROTI>2 (right), bottom: ROTI>~~5~~5. Binsize 1° Mlat ×0.2 h MLT

Again a benefit from using the second derivative instead of the first derivative may be seen. The number of weighted/screened positions is similar~~too, maybe slightly smaller~~, but the difference and error degree amplitude is reduced, especially in the higher degrees, see ~~figure~~ Fig. 9. Also the geoid-RMS is reduced by ~~1.1mm~~ 1.1 mm for March 2015, which is a heavily affected month, see ~~table~~ Table 1.

4.4 Orbit

~~Analyzing~~ When analyzing the orbits, we see that ~~he~~ the differences between kinematic and reduced dynamic positions (see ~~figure~~ Fig. 11) are almost unaffected by the weighting. The spikes are still present even though their covariance information has changed as will be shown in Sect. 4.4 and Sect. 4.5. Low frequency differences are introduced due to ~~different~~ differently estimated empirical accelerations, which is caused by down-weighting ~~systematically affected~~ the problematic observations in the ~~least-square fit~~least-squares adjustment. This may be illustrated in particular by comparing the differences of the reduced dynamic orbits to the unweighted reference, see ~~figure~~ Fig. 12 (left). The comparison reveals low-frequency differences of up to

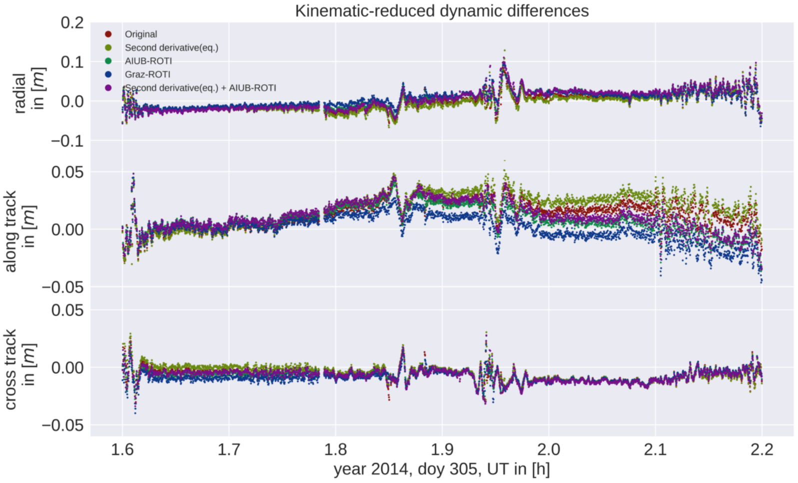

Figure 11. Kinematic minus reduced dynamic positions in radial, along- and cross-track direction. For both, kinematic and reduced dynamic positions, the same weighting was applied

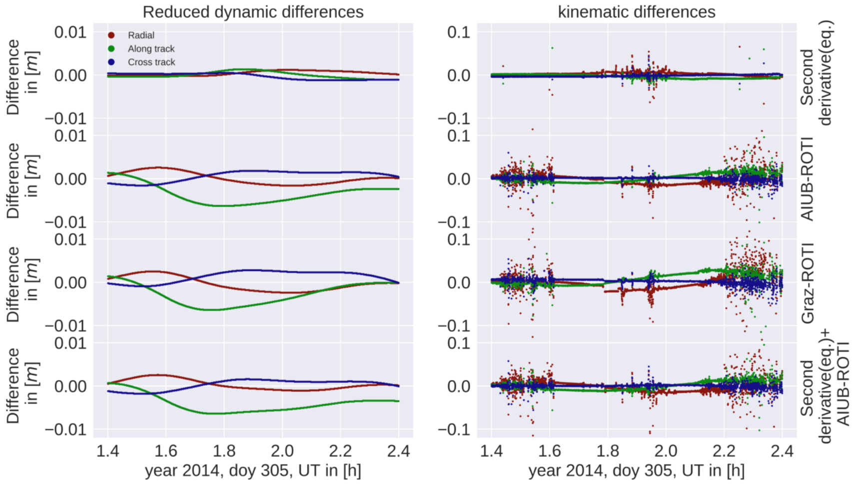

Figure 12. Differences between the unweighted positions of reduced dynamic (left) and kinematic (right) orbits. All ~~Orbits~~ orbits were compared to the unweighted case.

~~1cm amplitude~~ 1 cm amplitude for the ROTI-based approaches. Analyzing the kinematic positions on the right-hand side, one can see big differences around the polar regions and in the equatorial regions, too of up to ~~10cm~~10 cm. Such large ~~difference~~ differences are, however, only visible for very few epochs. In all four cases presented the differences are spatially very localized.

Considering the Graz-ROTI weighting, one can see a jump in the radial component and the along track component in the kinematic positions. This is an indicator, that the ~~scaling function introduces too largeweights~~sigma squares introduced by the scaling function are too large. Such jumps also occur at other epochs for the Graz-ROTI, but in a few cases they also ~~occure~~ occur in other weighting strategies, when large ~~weights~~ sigma squares are applied.

In all other cases the differences especially between the kinematic positions are very small in between the polar regions and the equatorial anomaly.

4.5 Covariances

The gravity field is not only determined by the used kinematic positions (pseudo-observations) but also by the adopted weights of the kinematic positions derived from their covariance information. To demonstrate how different the weighting schemes affect the covariance information of the kinematic positions, we analyze the covariances of the kinematic positions as a function of their geographic and geomagnetic locations, respectively. The information was binned (~~$1° lat \times 1° lon$ degree for geographic and $1° Mlat \times 0.2 h MLT$~~ 1° lat×1° lon for geographic coordinates and 1° Mlat×0.2 h MLT) and the mean of the radial variances, see ~~section 2.1~~Sect. 2.3, was computed. For better visibility the logarithm of that mean was taken. As ~~already mentioned,~~ one can see that for the AIUB standard screening ~~the covariances~~ high radial variances are a single band along the geomagnetic equator, compare ~~figure~~ Fig. 14 and 15 top, left. ~~The~~ A ground track is visible in the radial variances. This is connected to the Swarm A orbit on 20/03/2015. On this day the L1 RMS of the kinematic orbit is 0.022108 m, which is apporximately ten times the usual RMS. This is due to many screened observations and in turn short observation pieces. For comparison: using the second derivative weighting in addition to the AIUB-ROTI for the same day the L1 RMS is 0.001478 m. The other positions below and above the equator ~~don't show big~~ do not show high covariances, but ~~they are~~ the number of positions is significantly decreased as ~~figure~~ Fig. 13 illustrates. Between the two ~~peaks~~ bands the geometry of the observations is weakened resulting in high variances. In the two bands too many observations are affected by the screening, resulting in a significant loss of positions. For the ~~second derivative based~~ combined weighting approach, we see two bands around the geomagnetic equator, compare with ~~figure~~ Fig. 14 and 15 bottom right. The positions ~~in between~~ between the two bands are of significantly better quality as the positions obtained using AIUB standard screening. As mentioned for the ROTI approaches, highest variances are resulting for areas of fluctuations such as the poles and equatorial ~~region~~ regions around 18-22 MLT, which are well-known for equatorial plasma bubbles. This may be well recognized when plotting the covariances in geomagnetic coordinates (~~figure~~ Fig. 15). Using the second derivative in addition to the ROTI (bottom right) results in higher covariances in the ~~tow~~ two bands around the geomagnetic equator, also higher covariances in earlier LT may be recognized. This illustrates the different sensitivities of the two approaches.

~~The covariance information plays an important role for the gravity field processing (Prange et al., 2009). It is is used for weighting in the least square adjustment. If systematically biased positions have high covariance, their impact on the gravity field gets automatically reduced.~~

4.6 Validation

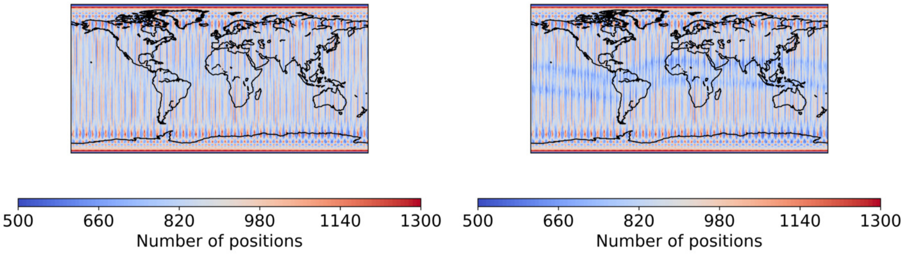

Figure 13. ~~Absolute number~~ Number of kinematic positions for the analyzed test period, un-screened (left) and with AIUB standard screening (right). Binned in $1^\circ \times 1^\circ$ grid.

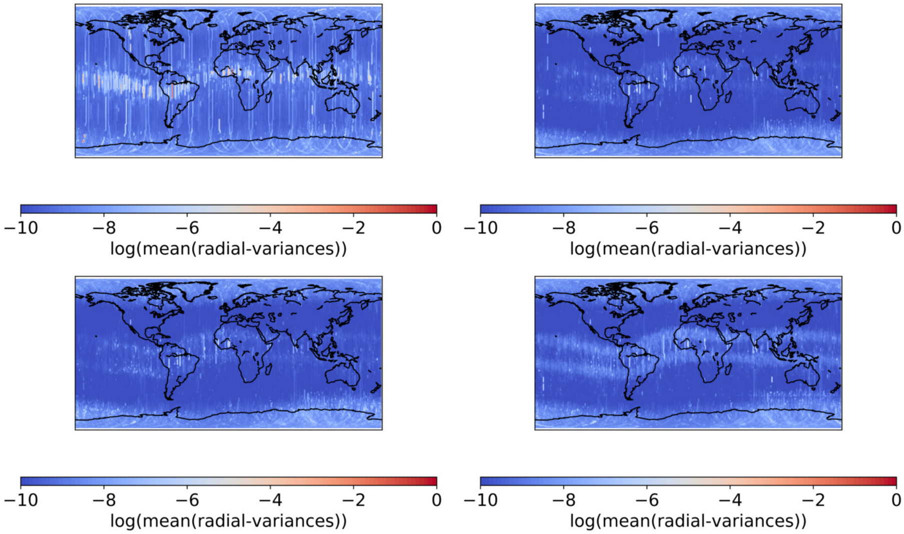

Figure 14. ~~Kinematic Variances~~ Radial variances for the analyzed test period, global. Top: AIUB standard screening (left), AIUB-ROTI (right), bottom: ~~GRAZ-ROTI~~ Graz-ROTI (left), second derivative (eq.)+AIUB-ROTI (right). The clearly visible ground track (top, left) is due to a large RMS for Swarm A, 03/29/2015

~~As~~ For an independent validation of the obtained orbits, we use ~~satellite laser ranging~~ Satellite Laser Ranging (SLR) measurements and compute the differences between the SLR-measurement and the GPS-based computed distances. As ~~Additional~~ SLR Stations high-quality stations Graz (GRZL), Greenbelt (GODL), Haleakala (HA4T), Hartebeesthoek (HARL), Herstmonceaux (HERL), Matera (MATM), Mt Stromlo (STL3), Potsdam (POT3), Wettzell (SOSW), Wettzell (WETL), Yarragadee (YARL) and Zimmerwald (ZIML) are selected following the approach of Jäggi et al. (2016). An outlier threshold of 20 cm and an elevation-cutoff of 10° was applied. For March 2015 approximately 1400 normal points, and for June 2016 1300 normal points are available. As additional criteria we use the L1-phase RMS of the ~~orbit of the GPS data, the~~ gravity field adjustment, the cos of latitude weighted RMS of the geoid height differences with respect to a superior solution based on ultra-precise GRACE

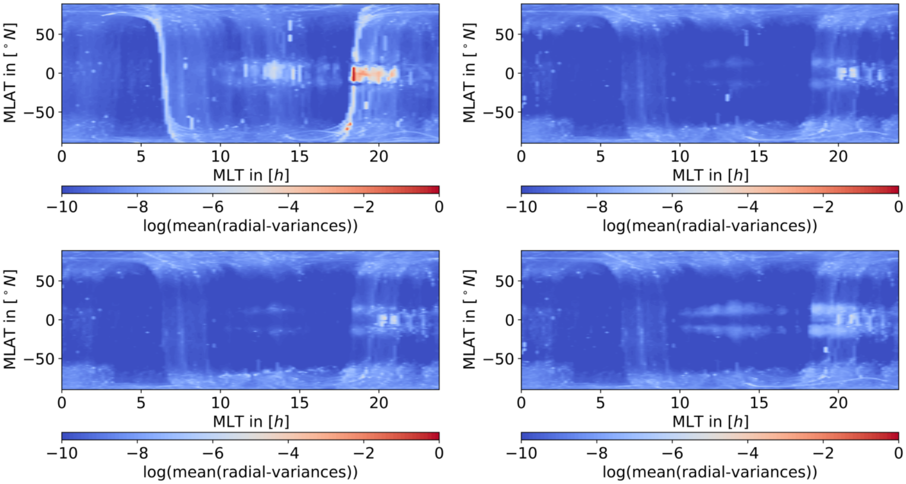

Figure 15. ~~Kinematic Variances~~ Radial variances in magnetic coordinates. Top: AIUB standard screening (left), AIUB-ROTI (right), bottom: ~~GRAZ-ROTI~~ Graz-ROTI (left), second derivative (eq.)+AIUB-ROTI (right)

~~K-Band~~ K-band measurements, and the ~~(~~cos of latitude ~~)~~ weighted standard deviation above the ocean (Meyer et al., 2012), see ~~table~~ Table 1 and 2. It is interesting that we could preserve more positions in the ~~weighted case~~ ROTI weighted cases than in the case without weighting, now being kept ~~in the system~~ with lower weight. The geoid RMS of the gravity field solutions using unscreened and screened ~~soulutions~~ GPS observations is at the same level as the values published in (Dahle et al., 2017). In the weighted scenarios for March 2015, the geoid RMS is reduced when using the second derivative for weighting or when combining the second derivative derived weights with the ~~ROTI 1~~ AIUB-ROTI derived weights. For June 2016 the second derivative derived based weights lead to ~~a small degradation of the~~ no differnce in geoid RMS . For this month we obtain the smallest geoid RMS when using ROTI derived weights. For both months the geoid RMS obtained when using the combination of the ~~ROTI 1~~ AIUB-ROTI derived weights and the second derivative derived weights is among the lowest. The ROTI approaches again tend to reduce the noise, which may be seen in the reduction of the geoid RMS, even if the geoid RMS for ~~march~~ March 2015 is slightly bigger compared to the second derivative. This might be due to the still existing artifacts around the geomagnetic equator. The fact that this improves significantly by combining the AIUB-ROTI with the second derivative supports this assumption. The same effect is visible for the weighted standard deviation above the oceans.

~~The~~ Regarding SLR, the mean offsets, as well as the standard deviations ~~are at the same level in~~ for the reduced dynamic ~~case. In the kinematic cases~~ orbits stay on a similar level. For the kinematic orbits the mean and SLR standard deviations show a slight improvement if the ROTI approach is used.

In June 2016 the validation improves, but the orbits in June 2016 are not that much affected by the ionospheric activity. This is due to the less critical local times and a reduced ~~solar Flux~~ F10.7 index, which indicates less ionospheric activity, compare with ~~figure 10 and table~~ Fig. 10 and Table 4. But even in that case the ROTI approaches seem to be capable to improve the mean of the SLR residuals for the kinematic positions.

Table 1. Statistics and SLR-Residuals for Swarm A, March 2015

Scenario	# Kin. Pos.	L1 RMS [mm]	Geoid RMS [mm]	wStd Ocean [mm]	RD mean (SLR)[mm]	RD std (SLR)[mm]	KN mean (SLR)[mm]	KN s (SLR)[
Original	696060	2.78	~~22.0~~ 21.6	101.2	4.6	27.3	2.4	31.1
Std. scr. $dL4/dt$	636633	2.75	~~13.8~~ 13.6	63.7	3.7	26.9	0.7	31.4
Wgt. $dL4/dt$	689895	2.65	13.1	67.4	4.6	27.6	2.0	32.7
Wgt. d^2L4/dt^2, eq.	693648	2.64	~~12.9~~ 12.4	62.1	4.6	27.3	1.9	32.5
Wgt. ~~ROTI 1~~ AIUB-ROTI	700503	2.18	~~14.3~~ 13.8	64.5	4.9	26.5	1.0	28.8
Wgt. ~~ROTI 2~~ Graz-ROTI	700155	2.11	~~14.1~~ 13.6	61.7	~~5.0~~ 5.0	25.8	~~0.9~~0.9	28.7
Wgt. ~~ROTI 1~~ AIUB-ROTI + 2nd der.	700569	2.14	~~12.5~~ 12.0	55.3	5.0	26.0	0.6	29.3

Table 2. Statistics and SLR-Residuals for Swarm A, June 2016

Scenario	# Kin. Pos.	L1 RMS [mm]	Geoid RMS [mm]	wStd Ocean [mm]	RD mean (SLR)[mm]	RD std (SLR)[mm]	KN mean (SLR)[mm]	KN s (SLR)[
Original	783996	2.03	~~8.6~~8.3	~~45.7~~45.3	3.3	14.0	1.7	16.4
Std. scr. $dL4/dt$	783153	2.01	~~9.1~~8.8	~~47.0~~46.6	3.2	14.2	1.7	16.6
Wgt. $dL4/dt$	783822	1.95	8.25	46.6	3.2	14.1	1.6	16.5
Wgt. d^2L4/dt^2, eq.	783714	2.01	~~8.9~~8.3	~~46.9~~46.6	3.3	14.0	1.7	16.4
Wgt. ~~ROTI 1~~AIUB-ROTI	784182	1.70	~~7.3~~7.0	~~37.9~~37.4	3.4	14.1	1.4	16.5
Wgt. ~~ROTI 2~~Graz-ROTI	784209	1.64	~~7.4~~7.1	~~39.7~~39.2	3.4	14.2	1.4	16.4
Wgt. ~~ROTI 1~~ AIUB-ROTI + 2nd der.	784128	1.69	~~7.4~~7.1	~~38.9~~38.4	3.3	14.2	1.3	16.7

4.7 Weighted observations and $F10.7$ ~~-Index~~index

As shown by Jäggi et al. (2016) the amount of screened or in our case weighted observations depends on the ionospheric activity. ~~(Jäggi et al., 2016)~~ The authors used the TEC ~~content~~ to demonstrate this. For our study, we compare the number of weighted observation to the $F10.7$ ~~-Index~~ index as well as the Kp ~~-Index~~index. The first one is an indicator for the ionization, whereas the second is an indicator for the geomagnetic activity. As shown by Stolle et al. (2006), the probability of an equatorial plasma bubble is ~~positive~~ positively correlated to the $F10.7$ ~~-Index~~index. Equatorial plasma bubbles usually occur, when there is a high activity in the ionosphere. Previous studies connect bubbles to a strong vertical ~~pre reversal~~ prereversal enhancement, fast changes in plasma density, an unstable E-F boundary, and strong gradients (Whalen (2000), Kelley (1989a), Stolle et al. (2006)). This is of course harmful to the quality of GPS-data as one can see in ~~figure~~ Fig. 3 (left), where especially the bubble region shows high variances. So we expect a correlation between the $F10.7$ ~~-Index~~ index and the number of weighted observations.

Figure 16. Percentage of screened position in comparison to the $F10.7$ and Kp ~~Indexes~~indices

Secondly the Kp ~~Index~~ index represents the disturbances in the geomagnetic field. Because the motion of ionospheric plasma is connected to the magnetic field (Kelley, 1989b), disturbances in the magnetic field may result again in errors in kinematic positioning. So we expect again a high number of affected observations under storm conditions. These comparisons are illustrated in ~~figure~~ Fig. 16. To avoid contamination due to the polar regions, we limit all three data sets to the equatorial regions (lat$<50°$). The largest daily averaged Kp ~~Index in our Time~~ index in our time series is 6 on day ~~15076~~ $2015-076$ (03/17/2015). On this day, there was a severe magnetic storm (class G4) with Kp up to $8-$. Especially in the second and third time derivative based weighting one can see a clear increase in the relative number of affected epochs. Most probably this is related to increased ionospheric fluctuations as they occur in storm conditions. In total the percentage of weighted observations shows a similar behavior as the $F10.7$ ~~Index~~index. Some differences can be explained by the local time dependence. In total, as one can see in ~~table 3that~~ Table 3, the correlation between the percentage of weighted observations and the $F10.7$ ~~Index~~ index is quite strong (above 0.7) for Swarm A and Swarm C, but a lot weaker for Swarm B. The reason might be the higher altitude of Swarm B which leads to less free electrons and weaker gradients in the ray paths to the GPS-satellites. In addition, Swarm B passes on different local times. For march 2015 the local times are comparable, resulting in a very similar behavior (see fig. 16). ~~Toward~~ Towards the last months (July and August 2016) the local time of Swarm B is ~~significant~~ significantly different from the critical ~~regions~~ local times $(18LT-02LT)$, but in the same months Swarm A and Swarm C are inside the critical local times. Here we can clearly see the peak of the $F10.7$ ~~Index~~ index around day 200 in the percentage of weighted observations for Swarm A and Swarm C but ~~nothing~~ no signature is visible for Swarm B.

Table 3. Correlation coefficient between the relative number of weighted observations and the $F10.7$ ~~index~~index

Method	D1 (eq.)	D2 (eq.)	D3 (eq.)
Swarm A	0.7025	0.7313	0.7564
Swarm B	0.3005	0.46400	0.6766
Swarm C	0.7925	0.7914	0.8219

Table 4. Local ~~Time~~ time at middle of month

Month	Jan.'15	Mar.'15	Feb.'16	Mar.'16,	Jun.'16	Jul.'16	Aug.'16
Swarm A, C	$\sim 1LT, 13LT$	$\sim 8LT, 20LT$	$\sim 2LT, 14LT$	$\sim 11LT, 23LT$	$\sim 3LT, 15LT$	$\sim 0LT, 12LT$	$\sim 9LT, 21LT$
Swarm B	$\sim 2.5LT, 14.5LT$	$\sim 9LT, 21LT$	$\sim 5LT, 17LT$	$\sim 2LT, 14LT$	$\sim 6LT, 18LT$	$\sim 3LT, 15LT$	$\sim 0LT, 12LT$

5 Conclusions

We showed that ~~spikes in the kinematic positioning, as they occur in the obit processing of the Swarm Mission,~~ systematic errors up to 10 cm in difference between kinematic positions and a reduced dynamic orbit are associated to sharp peaks in the plasma density. These errors propagate into the gravity field solutions derived from kinematic positions. When validating the monthly Swarm GPS-only gravity field solution to the corresponding JPL-GRACE-RL06 solution, band shaped resiuals up to 4 cm in geoid height become visible. Furthermore, we showed that these ~~spikes have~~ systematics are associated with large phase residuals of $4-6$ cm and can be identified using time derivatives of the geometry-free linear combination. Based on these time derivatives we developed weighting criteria and used already existing techniques such as the ROTI approach and the AIUB standard screening. We found that the second derivative based weighting ~~located around the equator~~ is very efficient in removing the ~~artifact~~ artifacts around the geomagnetic equator. The ROTI approach improved the gravity fields in the polar regions. Eventually we evaluated the different screening approaches and combined ~~them~~ the ROTI approach with the derivative based weighting to an even more effective approach. The improvement of the orbits is visible in the gravity fields as well as in the SLR residuals. For a heavily affected month (March 2015) the geoid RMS was improved form 21.6 mm to 12.0 mm and the standard deviation of SLR residuals for the kinematic orbits was improved form 31.1 mm to 29.3 mm. How different the weighting strategies apply to the observations is also visible in the covariance information of the kinematic positions. In turn this covariance information is essential to improve the gravity field solutions. The number of weighted observations, especially in the derivative based cases ~~seems to correlate~~ has a significant correlation coefficient, between 0.70 and 0.82, to the $F10.7$ ~~Index~~ index representing the ionospheric activity, which is consistent to previous studies (Jäggi et al. (2016) and Xiong et al. (2016)).

Data availability. The Swarm RINEX files are available via ESA's anonymous ftp: ftp://swarm-diss.eo.esa.int/
For the computation of the precise orbit the CODE final clock and GPS orbit pruducts were used. They are available via AIUB's anonymous ftp: ftp://ftp.aiub.unibe.ch/
The monthly GRACE-RL06 Gravity field solutions are available via JPL's anonymous ftp: ftp://podaac-ftp.jpl.nasa.gov/allData/grace/L2/JPL/RL06

Competing interests. The authors declare that they have no conflict of interest

Acknowledgements. This research project was funded by the Swiss National Science Foundation (SNSF) grant 200021_169035 Low Earth Orbiters and the Ionosphere's Stochastic Properties. Part of this study was also performed in the frame of ESA/DISC funded projects (contract SD-ITT-1.1, part of 000109587/13/I-NB) and in the frame of the Swarm Quality Working Group (QWG), which is organized by ESA. The Authors would also like to thank the editor and the two anonymous reviewers for their very precise and useful comments.

References

Beutler, G., Jäggi, A., Mervart, L., and Meyer, U.: The celestial mechanics approach: theoretical foundations, Journal of Geodesy, 84, 605–624, https://doi.org/10.1007/s00190-010-0401-7, 2010.

Bock, H., Jäggi, A., Beutler, G., and Meyer, U.: GOCE: precise orbit determination for the entire mission, Journal of Geodesy, 88, 1047–1060, https://doi.org/10.1007/s00190-014-0742-8, 2014.

Dach, R., Lutz, S., Walser, P., and (Eds), P. F.: Bernese GNSS Software Version 5.2 User manual, Astronomical Institute, University of Bern, Bern Open Publishing, 2015.

Dahle, C., Arnold, D., and Jäggi, A.: Impact of tracking loop settings of the Swarm GPS receiver on gravity field recovery, Advances in Space Research, 59, 2843 – 2854, https://doi.org/10.1016/j.asr.2017.03.003, 2017.

Gurtner, W. and Estey, L.: RINEX, The Receiver Independent Exchange Format, Version 3.00, IGS Data Format description, ftp://igs.org/pub/data/format/rinex300.pdf, 2007.

Jäggi, A., Bock, H., Meyer, U., Beutler, G., and van den IJssel, J.: GOCE: assessment of GPS-only gravity field determination, Journal of Geodesy, 89, 33–48, https://doi.org/10.1007/s00190-014-0759-z, 2015.

JPL/NASA: https://grace.jpl.nasa.gov/data/data-updates/, from 19. December 2017, last access: 21. September 2018, GRACE Data Updates, 2017.

JPL/NASA: https://www.jpl.nasa.gov/news/news.php?feature=7276, November 1, 2018, last access: 21. November 2018, JPL News, 2018.

Jäggi, A., Bock, H., Prange, L., Meyer, U., and Beutler, G.: GPS-only gravity field recovery with GOCE, CHAMP, and GRACE, Advances in Space Research, 47, 1020 – 1028, https://doi.org/10.1016/j.asr.2010.11.008, 2011a.

Jäggi, A., Prange, L., and Hugentobler, U.: Impact of covariance information of kinematic positions on orbit reconstruction and gravity field recovery, Advances in Space Research, 47, 1472 – 1479, https://doi.org/10.1016/j.asr.2010.12.009, 2011b.

Jäggi, A., Dahle, C., Arnold, D., Bock, H., Meyer, U., Beutler, G., and van den IJssel, J.: Swarm kinematic orbits and gravity fields from 18months of GPS data, Advances in Space Research, 57, 218 – 233, https://doi.org/10.1016/j.asr.2015.10.035, 2016.

Kelley, M. C.: Chapter 4 - Equatorial Plasma Instabilities, in: The Earth's Ionosphere, edited by Kelley, M. C., pp. 113 – 185, Academic Press, https://doi.org/10.1016/B978-0-12-404013-7.50009-5, 1989a.

Kelley, M. C.: Chapter 2 - Fundamentals of Ionospheric Plasma Dynamics, in: The Earth's Ionosphere, edited by Kelley, M. C., pp. 23 – 63, Academic Press, https://doi.org/10.1016/B978-0-12-404013-7.50007-1, 1989b.

Lück, C., Kusche, J., Rietbroek, R., and Löcher, A.: Time-variable gravity fields and ocean mass change from 37 months of kinematic Swarm orbits, Solid Earth, 9, 323–339, https://doi.org/10.5194/se-9-323-2018, 2018.

Meyer, U., Jäggi, A., and Beutler, G.: Monthly gravity field solutions based on GRACE observations generated with the Celestial Mechanics Approach, Earth and Planetary Science Letters, 345-348, 72 – 80, https://doi.org/10.1016/j.epsl.2012.06.026, 2012.

Pi, X., Mannucci, A. J., Lindqwister, U. J., and Ho, C. M.: Monitoring of global ionospheric irregularities using the Worldwide GPS Network, Geophysical Research Letters, 24, 2283–2286, https://doi.org/10.1029/97GL02273, 1997.

Prange, L., Jäggi, A., Beutler, G., Dach, R., and Mervart, L.: Gravity Field Determination at the AIUB – The Celestial Mechanics Approach, in: Observing our Changing Earth, edited by Sideris, M. G., pp. 353–362, Springer Berlin Heidelberg, Berlin, Heidelberg, 2009.

Stolle, C., Lühr, H., Rother, M., and Balasis, G.: Magnetic signatures of equatorial spread F as observed by the CHAMP satellite, Journal of Geophysical Research: Space Physics, 111, https://doi.org/10.1029/2005JA011184, 2006.

van den IJssel, J., Forte, B., and Montenbruck, O.: Impact of Swarm GPS receiver updates on POD performance, Earth, Planets and Space, 68, 85, https://doi.org/10.1186/s40623-016-0459-4, 2016.

Whalen, J. A.: An equatorial bubble: Its evolution observed in relation to bottomside spread F and to the Appleton anomaly, Journal of Geophysical Research: Space Physics, 105, 5303–5315, https://doi.org/10.1029/1999JA900441, 2000.

Xiong, C., Stolle, C., and Lühr, H.: The Swarm satellite loss of GPS signal and its relation to ionospheric plasma irregularities, Space Weather, 14, 563–577, https://doi.org/10.1002/2016SW001439, 2016.

Zehentner, N. and Mayer-Gürr, T.: Mitigation of ionospheric scintillation effects in kinematic LEO precise orbit determination, EGU General Assembly 2015, 2015.